Lithium fluoride/iron difluoride composite prepared by a fluorolytic sol–gel method: Its electrochemical behavior and charge–discharge mechanism as a cathode material for lithium secondary batteries

Shinya Tawa,[a] Yuta Sato,[b] Yuki Orikasa,[c] Kazuhiko Matsumoto,*[,a] Rika Hagiwara [a]

[a] *Graduate School of Energy Science, Kyoto University, Yoshida-honmachi, Sakyo-ku, Kyoto 606-8501, Japan*

[b] *Nanomaterials Research Institute, National Institute of Advanced Industrial Science and Technology (AIST), 1-1-1 Higashi, Tsukuba, Ibaraki 305-8565, Japan*

[c] *Department of Applied Chemistry, College of Life Sciences, Ritsumeikan University, 1-1-1 Noji-higashi, Kusatsu, Shiga 525-8577, Japan*

*Corresponding author

E-mail: k-matsumoto@energy.kyoto-u.ac.jp (K. Matsumoto)

Tel: +81-75-753-5827

Fax: +81-75-753-5906

Abstract

Owing to their high theoretical capacity, metal fluorides have attracted significant interest as materials for fabricating the cathode of lithium secondary batteries. In the present study, a nanocomposite of LiF and FeF_2 is prepared by a fluorolytic sol–gel method in an ethanol solution, for use as the cathode material of a lithium secondary battery. The produced LiF/FeF_2 composite is characterized by broad X-ray diffraction peaks attributed to the nanosized (~10 nm) LiF and FeF_2 crystals, a large Brunauer–Emmett–Teller surface area of 119 m^2g^{-1}, and adsorption–desorption hysteresis, attributed to the presence of mesopores. The results of charge–discharge tests indicates an initial discharge capacity of 225 mAh (g-LiF/FeF_2)$^{-1}$ through reversal conversion at a current rate of 10 mA (g-LiF/FeF_2)$^{-1}$. Based on a combination of galvanostatic intermittent titration, X-ray absorption, and X-ray diffraction investigations, a new reaction mechanism is developed, namely, the conversion of the local environment of an Fe atom from a rutile-type FeF_2 structure to a rhenium trioxide-type FeF_3 structure during charging, with the subsequent discharge resulting in the insertion of Li^+ into the rhenium trioxide-type FeF_3 structure, followed by the conversion reaction to LiF and FeF_2.

Keywords:
fluoride, reversal conversion, galvanostatic intermittent titration technique, x-ray absorption spectroscopy, nanocomposite

1. Introduction

Recent years have witnessed the application of lithium ion battery (LIBs) technology to electric vehicles, in addition to consumer electronics.[1-4] LIBs are expected to be further used for the large-scale storage of surplus electricity generated from renewable energy sources, and this would require the achievement of an energy density higher than the present level.[5, 6] However, the materials currently used for the cathode of LIBs have a lower capacity compared with the anode materials, resulting in a limitation of the energy density of the whole battery and an urgent need for improved performance.[7-11]

Polyanionic compounds such as $LiFePO_4$ are presently being investigated for use as cathode materials in addition to the widely utilized layered oxides. These materials have good charging and discharging cycle performances, utilizing lithium insertion/desertion reactions in a stable polyanion framework.[7, 12] However, their theoretical capacity is restricted by the polyanion occupying a large volume in the crystal structure. Owing to their high theoretical capacity, transition metal fluorides have attracted attention for use as cathode materials.[13-19] Such compounds are composed of a metal element and a small, light fluoride ion and thus have a high theoretical capacity with respect to their mass and volume. A higher redox potential compared with the

corresponding oxides is also expected owing to the inductive effect of the fluoride ion. Among the available fluoride candidates, the abundant sources and low toxicity level of FeF_3 and its related compounds make them particularly attractive as LIB electrode materials.[13-18, 20-36]

There have been previous reports of the fabrication of composites containing carbonaceous materials [14, 24, 30] and with controlled crystallinity [26] and nanonization [23, 31], all of which enabled significant improvement of the electrode performance of FeF_3. A three-electron capacity of 712 mAh g^{-1} has been obtained for FeF_3, with the conversion reaction involving the formation of metallic iron and lithium fluoride. However, the complete utilization of the conversion reaction requires discharge to ~1.0 V vs. Li^+/Li, which has so far been a challenge in practical application. Although limited usage of the redox region of a one-electron reaction (Fe^{III}/Fe^{II}) reduces the capacity, it affords a reasonably high average discharge potential of ~3 V vs. Li^+/Li, with the theoretical capacity still being sufficiently high at 237 mAh g^{-1}. Several reaction mechanisms have been proposed for this system with respect to the characteristics of the starting FeF_3 material.[21] For example, Some literature reported a lithium insertion reaction proceeds from FeF_3 to $LiFeF_3$ through the formation of solid solution when nanosized FeF_3 is used.[22, 28, 31, 32, 34] There has also been the suggestion that

$Li_{0.5}FeF_3$ with a trirutile structure is formed as an intermediate phase, with further lithiation occurring by single-phase reaction based on the trirutile $Li_{0.5}FeF_3$ structure.[22] It has, however, also been proposed that the conversion reaction to LiF and FeF_2 occurs in the latter half of the one-electron reaction.[34]

The absence of lithium in FeF_3 constitutes a drawback for the practical application of the fluoride, because an LIB can be fabricated only with an anode that does not contain lithium, such as a graphite electrode. Reversal conversion from Fe^0 [37] or $Fe^{II}F_2$ [38] using LiF is a practical method for addressing this issue. Although the chemical synthesis of a lithium-containing material such as $LiFeF_3$ is a suitable approach when starting from Fe^{II}, the material would not only occur as a metastable phase, but the practical implementation of the synthesis has so far been unsuccessful. The alternative use of a LiF/FeF_2 composite has been investigated.[38] The LiF/FeF_2 nanocomposite was prepared by ball-milling and found to have a large reversible capacity of 190 mAh g^{-1}, with a reversible charge–discharge reaction proposed to occur via the formation of $Li_{0.5}FeF_3$. However, ball milling is unsuitable for mass production and contamination from the ball and container is liable to occur. There is thus the need for an alternative method for synthetizing the LiF/FeF_2 composite.

In the present study, the preparation of a LiF/FeF_2 nanocomposite as a Fe^{II} source

using the one-electron reaction of iron and a fluorolytic sol–gel method was investigated. Although the fluorolytic sol–gel method is commonly used for the preparation of metal fluoride nanoparticles for catalytic and optical applications, offering the advantage of a large reactive surface,[39, 40] it has also been applied to the production of battery electrode materials, albeit limitedly.[41-44] The LiF/FeF_2 composite powder prepared in the present study was characterized by X-ray diffraction (XRD), field emission scanning electron microscopy (FE-SEM), and nitrogen adsorption analysis. Its reaction mechanism was also analyzed by XRD, transmission electron microscopy (TEM), and X-ray absorption spectroscopy (XAS). Galvanostatic intermittent titration technique (GITT) measurement was also carried out to investigate the voltage relaxation behavior during the charge–discharge.

2. Experimental

2.1 Reagents

The utilized volatile materials were handled in a vacuum line constructed from stainless steel, Pyrex glass, and tetrafluoroethylene-perfluoroalkylvinylether copolymer (PFA). The nonvolatile materials were handled in a dry argon atmosphere in a glove box or in a dried-air atmosphere in an open dry chamber. Anhydrous hydrgen fluoride (HF,

Daikin Industries Co. Ltd.; purity > 99%)) was dried over K_2NiF_6 (Ozark-Mahoning Elf Atochem North America, Inc., purity: 97%) in a PFA reactor prior to use. Iron (II) acetate ($Fe(OAc)_2$, Sigma-Aldrich, Inc., purity > 99.99%), lithium acetate (Li(OAc), Sigma-Aldrich, Inc.; purity > 99.95%), ethanol (EtOH, Wako Pure Chemical Industries, Ltd.; purity > 99.8%, water content < 10 ppm) were used as received.

2.2 Preparation of the LiF/FeF_2 composite

An ethanol solution of HF was prepared by distilling 0.97 g of HF (48 mmol) onto 4.8 mL of ethanol. Metal acetates (0.320 g of Li(OAc) (4.85 mmol) and 0.844 g of $Fe(OAc)_2$ (4.85 mmol)) were dispersed in 25 mL of ethanol. The ethanol solution of HF was loaded into one arm of a T-shaped PFA reactor and slowly transferred onto metal acetates dispersed in ethanol, resulting in the immediate formation of a transparent red sol. The volatiles were removed over a period of 1 day under reduced pressure at 25°C, and subsequently at 100°C, resulting the formation of 0.568 g of red powder (theoretically 0.581 g for the formation of LiF and FeF_2).

2.3 Analyses

The samples of the prepared composite used for XRD investigation were placed

on a glass sample holder and the diffraction patterns were recorded by a powder X-ray diffractometer Smart Lab (Rigaku Corp.; Cu-Kα radiation, 40 kV-30 mA). All the samples were sealed in an air-tight cell with beryllium windows (purity > 97%) (Rigaku Corp.) filled with dry argon. Nitrogen adsorption analysis was performed using a Tristar II 3020 equipment (Shimadzu Corp.) to evaluate the surface area and pore-size distribution of the samples. The methods of Brunauer–Emmett–Teller (BET) [45] and Barrett–Joyner–Halenda (BJH) were respectively used for the evaluation of these two properties.[46] The morphology and composition of the samples were analyzed by a field-emission scanning electron microscope (Hitachi, SU-8020) and energy dispersion X-ray spectrometer (Hitachi). The samples used for TEM and XAS measurements were prepared by dismantling of the coin cells in a glovebox filled with dry argon after the charge–discharge test and washing of the cathode electrodes with dimethyl carbonate (Wako; H_2O < 20 ppm). The electrode film was peeled off from the Al mesh and vacuum-dried. Transmission electron microscopy and electron diffraction analyses were performed using a JEOL JEM-2100F equipment fitted with double EDS detectors (JEOL Centurio) with an electron accelerating voltage of 60 kV. For XAS measurements, the samples were thoroughly mixed with boron nitride (electrode film of ~5.7 mg, boron nitride of ~250 mg) and molded into pellets. The XAS measurements were performed using the beamline

BL14B2 at SPring-8 (JASRI, Japan) at room temperature. The Fe K-edge spectra were obtained in transmission mode. Fourier transformations were performed using k^3 weighting, and the local structural parameters were determined by curve-fitting using the REX2000 data analysis software.[47] The effective back-scattering amplitude $f(k, \pi)$ and the total phase shift φ were calculated using the multiple-scattering theoretical calculation program FEFF8.[48] The $\chi(k)$ function model was fitted using eq. (1):

$$\chi(k) = \sum_i \frac{N_i |f(k,\pi)| \exp\left(-2\sigma^2 k^2\right) \exp(-2R_i/\lambda_i) \sin\left(2kR_i + \phi_i(k)\right)}{kR_i^2} \quad (1)$$

where N is the number of neighboring atoms, R is the atomic distance to a neighboring atom, σ^2 is the Debye–Waller (DW) factor, and λ is the mean free path.

2.4 Electrochemical measurement

The LiF/FeF_2 composite was dry-milled with acetylene black (AB, Wako Pure Chemical Industries, Ltd.; purity > 99.99%) with a weight ratio of 70:25. A planetary ball mill with a zirconia vessel and zirconia balls (Fritsch, Pulverisette 7 Premium Line) was used for the milling, which was performed at a speed of 600 rpm for 1 h to obtain the LiF/FeF_2/AB composite. Powdered polytetrafluoroethylene (PTFE; Sigma-Aldrich, Inc.,

particle size: *ca.* 200 μm) was selected as a binder for the cathode. The LiF/FeF_2/AB composite and PTFE were well mixed with a weight ratio of 95:5 using an agate pestle and mortar until a homogeneous thin sheet was obtained. The weight ratio of LiF/FeF_2:AB:PTFE was 70:25:5, which follows the value in previous studies.[13,18] The sheet was pressed against an Al mesh under a pressure of 3 t cm^{-2} to form a cathode disk. Samples of the electrodes were tested by performing galvanostatic charge–discharge tests and GITT tests using 2032 coin-type cells. The cells were assembled in the Ar-filled glovebox using a 1 M $LiPF_6$/EC:DMC (1:1 volume ratio; Kishida Chemical Co. Ltd.; EC: ethylenecarbonate, DMC: dimethylcarbonate) electrolytic solution, glass-fiber filter separators (Whatman, GF/A; thickness 260 μm), and metal lithium foil counter electrodes pressed on stainless steel plates.

3. Results and discussion

Figure 1 summarizes synthesis and properties of the LiF/FeF_2 composites. Figure 1(a) illustrates the preparation of the LiF/FeF_2 composites under dry conditions (air and Ar) using the fluorolytic sol–gel method. The metal acetates were dispersed in ethanol and ethanoic solutions of anhydrous HF, respectively, and the two solutions were mixed and agitated until a homogeneous sol was obtained. The volatiles were then successively

removed in a vacuum to obtain the target composites. Figure 1(b) shows the XRD patterns of the obtained composite. The peak around $2\theta = 21°$ of the composite prepared in dry air is attributable to the strongest peak of the Fe^{III} complex salt Li_3FeF_6 (space group: $Pna2_1$ [49]), which was formed through the oxidation of Fe^{II} species by O_2 dissolved in ethanol. Conversely, the sample prepared in dry Ar only has peaks attributed to LiF (space group: *Fm*-3*m*) [50] and FeF_2 (space group: $P4_2/mnm$)[51], indicating the absence of impurities detectable by XRD. The peak width is comparable to that for a composite previously produced by ball-milling [38], suggesting similar crystallinity. The crystal size of the present LiF/FeF_2 composite sample was estimated to be 12 nm using the Scherrer equation [52], indicating a nano-level mixture of LiF and FeF_2, as has also been previously observed for other fluorides prepared by a fluorolytic sol–gel method [39, 40].

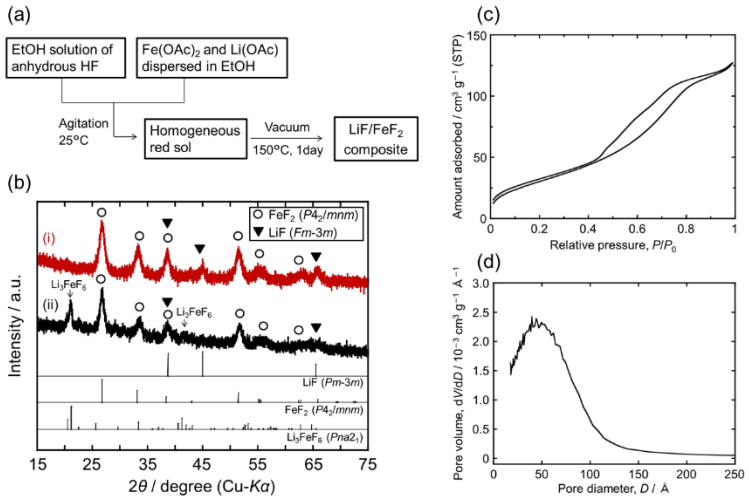

Figure 1 (a) Preparation of the LiF/FeF_2 composites using the fluorolytic sol–gel method (HF:$Fe(OAc)_2$:Li(OAc) ratio = 10:1:1) . (b) X-ray diffraction patterns of the LiF/FeF_2 composites prepared by the fluorolytic sol–gel method in (i) dry argon and (ii) dry air. (c)

Nitrogen adsorption–desorption isotherm and (d) BJH pore distribution of the LiF/FeF_2 composite prepared in dry Ar.

Figures 1 (c) and (d) shows the nitrogen adsorption–desorption isotherm of the LiF/FeF_2 composite prepared in dry Ar and the BJH pore-size distribution obtained from the isotherm. The hysteresis loop in the isotherm suggests the existence of mesopores, with its H2-type shape of the loop also suggesting the formation of micropores.[53] Using the BET method [45], the surface area of the composite was determined to be 119 $m^2 g^{-1}$. The surface area of nanosized fluorides produced by the fluorolytic sol–gel method depends on the utilized materials and the synthesis conditions, and the value for the present LiF/FeF_2 composite was observed to be smaller than those of typical AlF_3 and MgF_2 composites produced by the method (200–400 $m^2 g^{-1}$).[39, 40] The BJH pore size distribution of the nanopores of the present composite had a peak value of 5 nm, suggesting a nanoporous structure.

Figure 2 shows the FE-SEM images ((a) and (b)) and EDX mappings ((c) and (d)) of the LiF/FeF_2 composite, and the TEM images of the electrode film ((e) and (f)). Micro-ordered particles with rough surfaces can be observed in the low-magnification image (Figure 2(a)); the surface roughness originates from aggregation of nanoparticles smaller than 100 nm, as can be observed from the more magnified image (Figure 2(b)).

These FE-SEM observations reveal that the obtained composite consists of micro-sized secondary particles with mesopores formed by the aggregation of the nanoparticles, as also suggested by the BJH analysis above. The EDX analysis revealed Fe and F atoms uniformly distributed among these secondary particles, indicating homogenous mixing of FeF_2 and LiF at the micrometer level. The TEM observation further revealed the presence of 10-nm crystalline particles in the composite, with some of the lattice images indicating an interplanar distance of 0.28 nm, which corresponds to the *d*-spacing of the (101) plane of FeF_2.

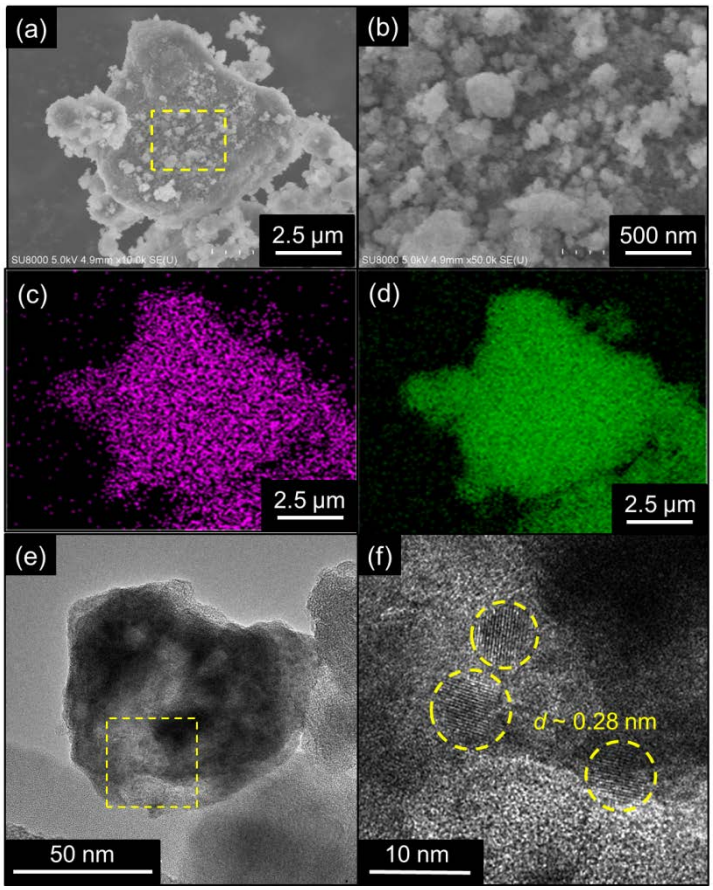

Figure 2 (a) Low- and (b) high-magnification FE-SEM images of the LiF/FeF_2 composite;

EDX mappings of (c) Fe and (d) F; and (e) low- and (f) high-magnification TEM images of the LiF/FeF_2 electrode film.

Figure 3 shows the charge–discharge performance of the LiF/FeF_2 composite electrode. The initial charge capacity is 235 mAh g^{-1}, while the discharge capacity is 225 mAh g^{-1}, which is close to the theoretical capacity of 227 mAh g^{-1}, giving an initial Coulombic efficiency of 96.6% (Figure 3(a)). The second charge curve does not overlap the initial charge curve, indicating a smaller polarization. A similar observation was made in a previous study that utilized a ball-milled sample.[38] A possible explanations for this behavior is a change from the dispersion state of the active material during the initial cycle. As can be observed from Figure 3(b), the reversible capacity of the electrode exceeds 190 mAh g^{-1} during the first 20 cycles. Although the Coulombic efficiency gradually increases with the number of cycles, it does not reach 99%, even on the 20th cycle. This is attributed to the continuous occurrence of side reactions such as the oxidative decomposition of the electrolyte during the charging process up to a relatively high potential of 4.8 V. After 20 cycles, significant degradation in capacity was observed. Although some more improvements are required for realization of long-cycle stability, the reversibility of 20 cycles is enough for the purpose of the present study, that is, clarification of the reaction mechanism for the LiF-FeF_2 system. Although the rate capability is an important

factor of an electrode material, there has been no previous report on it for LiF/FeF_2 composites. The present LiF/FeF_2 composite prepared by the fluorolytic sol–gel method was found to maintain 58% and 8% of its theoretical capacity at current rates of 200 mA g^{-1} (~1C rate) and 1000 mA g^{-1}, respectively. A previous study found that FeF_3 delivered 175 mA g^{-1} at a high current rate of 640 mA g^{-1} after heat treatment, which removed the stress in the crystal lattice, with the high crystallinity also maintained in subsequent charge–discharge cycles.[26] However, in the case of a LiF/FeF_2 composite, heat treatment of the host FeF_3 lattice before the preparation of the electrode is technically difficult.

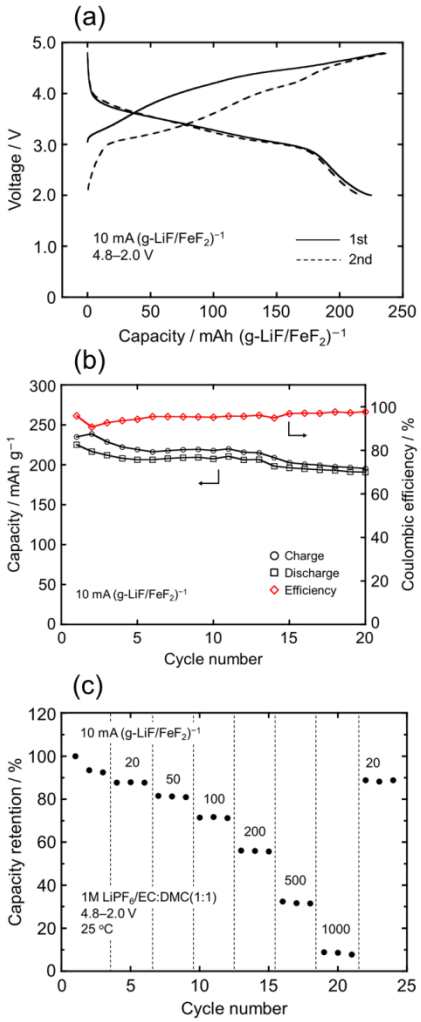

Figure 3 Charge–discharge performance of the LiF/FeF_2 composite electrode: (a) initial and second charge–discharge curves (10 mA g^{-1}); (b) capacity retention for the first 20 cycles (10 mA g^{-1}); and (c) rate capability based on the first cycle at 10 mA g^{-1} (10–1000 mA g^{-1}). Cut-off voltage: 2.0–4.8 V.

Figure 4 shows the results of tests that were used to investigate the polarization of the LiF/FeF_2 electrode during charge–discharge using the GITT. The GITT tests were used for repeated monitoring of voltage relaxation in the open circuit state immediately after charging or discharging to a certain level to clarify the polarization of the test

electrode. As can be observed from Figure 4(a), the voltage relaxation after 5 h gradually increases during the initial charging and converges to a constant value of about 4.2 V. However, as can be seen from Figure 4(b), and also noted earlier, the rate of the voltage relaxation is very low during charging. Conversely, small and fast voltage relaxation occurs over the entire range of discharge. The use of a longer relaxation time of 72 h also causes the relaxation potential during charging to be significantly higher than that during discharging (see Figure 4(c), for capacity vs. voltage). Furthermore, the voltage becomes nearly constant after 5 h during discharging, while the voltage relaxation during charging is very slow (Figure 4(d), for time vs. voltage). These observations strongly suggest that the equilibrium potential is practically approximated by the relaxed potential during discharging. Because the potential gradually decreases to ~3.0 V during discharging, a single-phase reaction is considered to occur in this region. The large voltage relaxation at the end of the discharge process also suggests that the reaction mechanism changes to another type such as a conversion reaction. Further details about this are presented under XAS analysis below. It would be difficult to analyze the electrode kinetics of iron fluoride systems by electrochemical impedance spectroscopy because of their slow relaxation leading to the difficulty to achieve the equilibrium state, as pointed out in a previous work.[32]

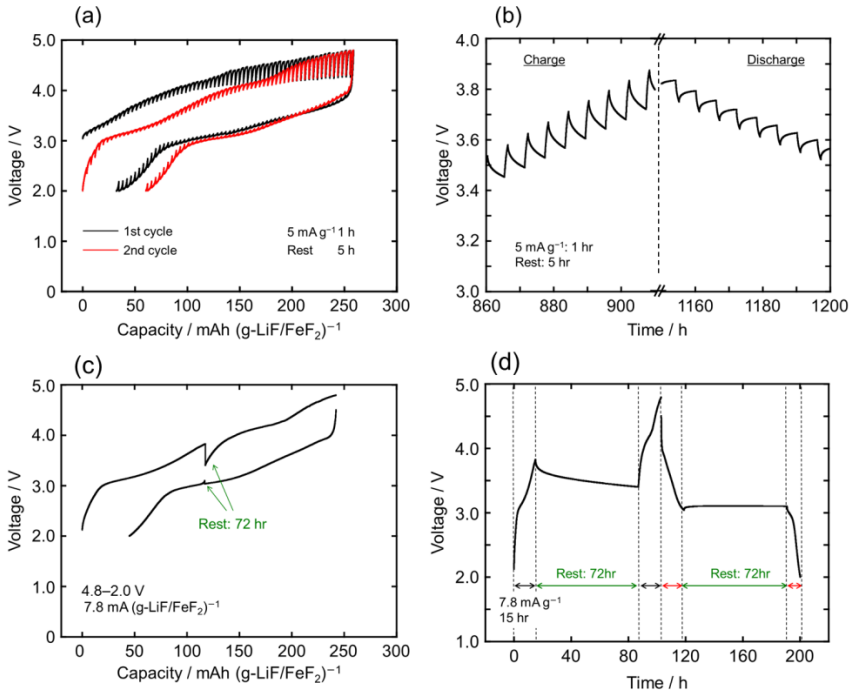

Figure 4 Voltage profiles of the LiF-FeF_2 composite electrode during galvanostatic pulse charge and discharge: (a) voltage–capacity and (b) voltage–time relationships (5 mA g^{-1} with 1-h and 5-h rests) and voltage decay curves with (72-h rest); and (c) voltage–capacity and (d) voltage–time relationships (7.8 mA g^{-1} for 1-h and 72-h rests).

Figure 5 shows the *ex situ* XRD patterns of the LiF/FeF_2 composite electrode during the initial charge–discharge cycle. The diffraction peaks of FeF_2 that are observed in the pristine electrode disappear after the initial charge, indicating the change of FeF_2 to other compounds by the charging reaction (Figures 5(a) and (b)). Although FeF_3 is expected to be generated during charging, no peaks of another compound such as FeF_3 are observed (Figure 5(b)). Nevertheless, amorphous FeF_3 may be generated by the reversal conversion reaction of LiF and FeF_2 during the initial charge. Although almost

no peaks are observed after the subsequent half discharge (Figure 5(c)), some weak peaks of FeF_2 reappear in the pattern for the fully discharged electrode (Figure 5(d)). These results suggest that, during the initial charge, LiF and FeF_2 react to form amorphous FeF_3, which is then converted back to LiF and FeF_2 after the subsequent discharge. However, the possible existence of the $Li_{0.5}FeF_3$ phase cannot be completely excluded based on only XRD results. This is because of the broadness of the XRD peaks and the similarity of the diffraction patterns of FeF_2 and $Li_{0.5}FeF_3$ (see discussion of the XAS data below).

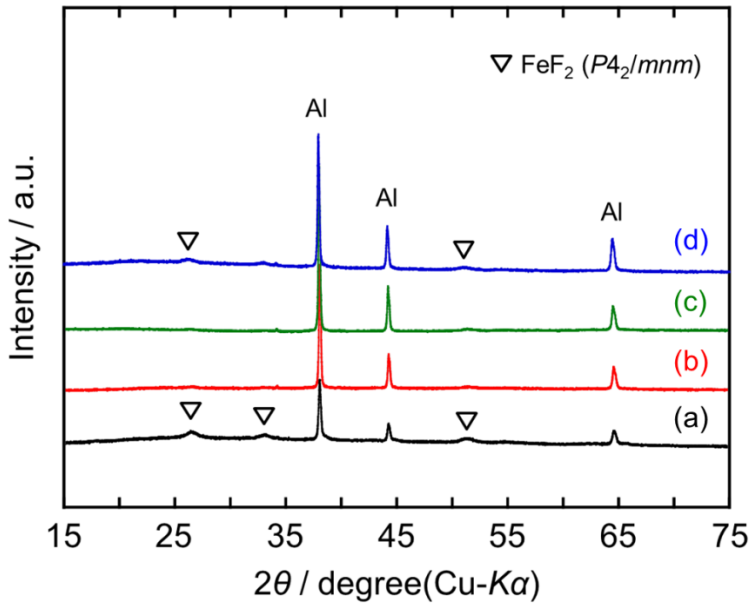

Figure 5 XRD patterns of the LiF/FeF_2 electrode in the (a) pristine, (b) charged, (c) half-discharged, and (d) discharged states. The peaks attributed to Al metal (current collector) are marked "Al".

Figure 6 shows the results of TEM and scanning TEM (STEM) examinations of

the LiF/FeF_2 electrode during the initial cycle. All the samples were observed to have almost the same morphology and Fe and F distributions. The pristine electrode had electron diffraction spots and rings attributable to FeF_2 (see Figures 6(a) and Figure S1 in Supplementary Data, for indexing). However, the diffraction rings were vague, in agreement with the low crystallinity observed in the XRD pattern. The FeF_2 diffraction spots almost disappeared after the initial charge (Figure 6 (b)), suggesting the vanishing of crystalline FeF_2 during the charge. The electron diffraction pattern of the fully discharged electrode also contained diffraction spots of FeF_2, suggesting the reformation of the compound during the discharge (see Figure 6(c) and Figure S2, Supplementary Data).

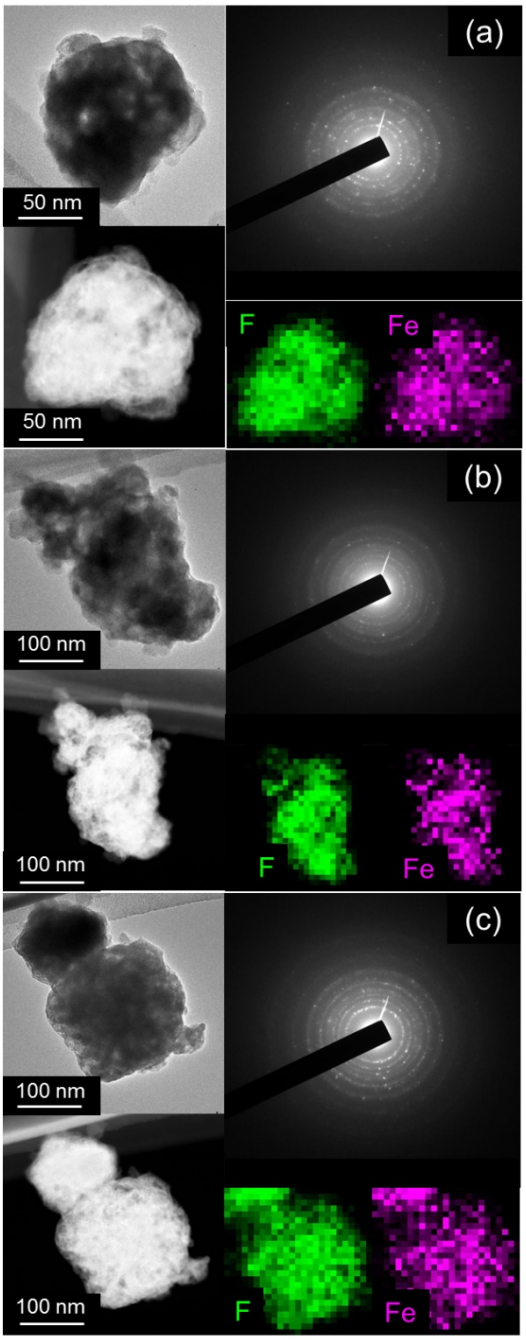

Figure 6 TEM and annular-dark field STEM images, EDX mappings of Fe and F, and electron diffraction patterns of the LiF/FeF_2 electrode in the (a) pristine, (b) charged, and (c) discharged states.

Figure 7 shows the results of the XAS investigation to examine the valence and bonding state of Fe in the electrode during the initial charge–discharge cycle. As can be

observed from the Fe K-edge X-ray absorption near edge structure (XANES) spectra in Figure 7(a), the absorption edge shifts to a higher energy after the initial charge, and then back to the original level after the subsequent discharge. The main peak in the transition metal K-edge XANES spectra corresponds to information about the oxidation state of the absorbing atom and the local geometric structure,[54] and it indicates redox activity between Fe^{II} and Fe^{III} and the recovery of the oxidation state and local structure around the Fe atom between the pristine and discharged states (see Figure S3, Supplementary Data, for the standard XANES spectra of FeO and Fe_2O_3). Fe K-edge EXAFS analysis was used to perform a detailed investigation of the local structure of the Fe atom. The Fourier transforms (FTs) of the EXAFS oscillations for the LiF/FeF_2 composite in the pristine, charged, and discharged states in Figure 7(b) reveal the radial distribution functions (RDFs) of the local environments around the Fe atoms (see Supplementary Data and Figure S4 for a detailed consideration of the data). The FT is significantly altered by the charging but returns to roughly the original form after discharging, with the first peak around 1.6 Å corresponding to the contribution of the Fe−F shell, and the second peak around 3.3 Å representing the contribution of the Fe−Fe and Fe−F shells. The distances differ from the crystallographic bond distance owing to the effect of the phase shift to radial structure functions. The refinement results of the pristine, charged, and discharged

LiF/FeF_2 composites are summarized in Table 1 (see Supplementary Data for the fitting details). The inverse FT obtained from the radial structure function of the pristine sample fitted well with the structural model based on the FeF_2 with the rutile structure (see Figure S5, Supplementary Data), in agreement with the XRD data above (Figure 5(a)). The primary Fe−F distance (~1.6 Å) was shortened by the charging process, explainable by the oxidation of Fe and the reduction of the ionic radius of the Fe ion between the divalent and trivalent states.[55] Fitting of the inverse FT of the charged sample with the structural model based on the distorted rhenium trioxide-type FeF_3 structure produced reasonable results (see Figure S6, Supplementary Data). However, the similar structures of the rutile-type FeF_2 and trirutile-type $Li_{0.5}FeF_3$ posed a difficulty to the XRD analysis of the discharged state, as state above. This implies two possibilities for the discharged state, namely, recovery of the original local environment of the rutile-type FeF_2 structure, or the further insertion of Li^+ into the trirutile-type $Li_{0.5}FeF_3$ structure. The fitting results of the inverse FT of the discharged sample showed that the residue of the rutile-type FeF_2 model (6.978%) was less than that of the trirutile-type $Li_{0.5}FeF_3$ model (8.858%) (see Figure S7 and Table S1, Supplementary Data), suggesting that conversion to LiF and FeF_2 was more plausible.

Table 1 Refinement results (bond distance, *R*, and Debye-Waller factor, σ) of EXAFS data of the LiF/FeF_2 composite at the pristine, charged, and discharged states.

Pristine state[a] (Residue: 4.598 %)			
Correlation	*CN*	*R* / Å	σ / Å
Fe-F	6	2.064(8)	0.116(10)
Fe-Fe	2	3.328(31)	0.106(30)
Fe-Fe	8	3.712(24)	0.123(18)
Fe-F	8	3.691(134)	0.172(190)

Charged state[a] (Residue: 8.438 %)			
Correlation	*CN*	*R* / Å	σ / Å
Fe-F	6	1.912(5)	0.110(7)
Fe-Fe	6	3.695(30)	0.136(25)
Fe-F	12	3.762(145)	0.200(165)

Discharged state[a] (Residue: 6.978%)			
Correlation	*CN*	*R* / Å	σ / Å
Fe-F	6	2.076(8)	0.128(10)
Fe-Fe	2	3.301(35)	0.110(30)
Fe-Fe	8	3.634(48)	0.151(75)
Fe-F	8	3.702(35)	0.084(28)

[a]The pristine, charged, and discharged models were fitted with the structural models based on the rutile FeF_2, rhenium trioxide FeF_3, and rutile FeF_2 structures, respectively. See Supplementary Data for details on fitting.

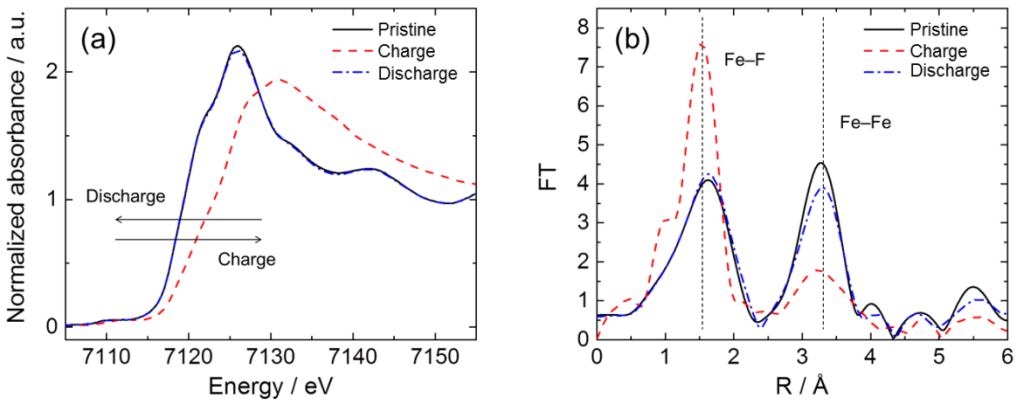

Figure 7 (a) XANES spectra and (b) Fourier transforms of the EXAFS oscillations of the LiF/FeF_2 electrode before the initial charge, after the charge, and after the following discharge.

Although the formation of FeF_3 was not confirmed by the XRD examination, the coordination state of Fe changed from that of FeF_2 to that of FeF_3 in the local region during the initial charge. These observations indicate that amorphous FeF_3 was formed by the charging process. All the XRD, ED, and XAS analyses confirmed the recovery of the FeF_2 crystallite after full discharge.

Table 2 briefly compares the previously known (charge-)discharge mechanisms of FeF_3 and LiF/FeF_2 as electrode materials with those determined from the present study. Figure 8 illustrates the reaction mechanism for the LiF/FeF_2 composite determined from the present study. Although some previous reports have claimed the formation of $Li_{0.5}FeF_3$ with a trirutile structure (t.r. in Table 2) as an intermediate phase during discharge from FeF_3 with a distorted rhenium trioxide structure (r.o. in Table 2) [22, 34],

the results of the present XRD analysis gave no indication of $Li_{0.5}FeF_3$ in the half-discharged state, as also supported by the absence of a plateau in the GITT measurements. The formation of $LiFeF_3$ by the insertion of Li^+ into the FeF_3 structure (distorted rhenium trioxide) or $Li_{0.5}FeF_3$ (trirutile) structure was also not observed. The local coordination state around the Fe atom changes back to that of FeF_2 after discharge, according to the XANES and EXAFS results. This supports the reaction mechanism suggested by the GITT measurements, namely, the initial occurrence of a single-phase reaction to form Li_xFeF_3 (r.o.), and a subsequent reaction at the end of discharge (x > ~0.8, based on the GITT measurements). The structure of the discharged state proposed in the present work differs from a previous submission,[38] even when the reaction begins from the reversal conversions of LiF and FeF_2 in both cases. This difference may be attributed to the differing characteristics of the starting materials, such as their particle sizes and crystallinities, as well as their preparation methods.

Table 2 Selected reaction mechanisms of FeF_3 and LiF-FeF_2 composite electrode material proposed in previous studies.

Starting material	Proposed discharge mechanism[a]	Reaction type	Ref
FeF_3 nano-particle (~15 nm)	(discharge) FeF_3(r.o.) + xLi$^+$ + xe$^-$ → Li$_x$$FeF_3$(r.o.)	Single-phase ($0 \le x \le 1$)	[31]
FeF_3 nano-particle (~8 nm)	(discharge) FeF_3(r.o.) + 0.5Li$^+$ + 0.5e$^-$ → Li$_{0.5}$$FeF_3$(t.r.)	Two-phase	[22]
	Li$_{0.5}$$FeF_3$(t.r.) + xLi$^+$ + xe$^-$ → Li$_{0.5+x}$$FeF_3$(t.r.)	Single-phase ($0 \le x \le 0.5$)	
FeF_3 nano-wire	(discharge) FeF_3(r.o.) + 0.5Li$^+$ + 0.5e$^-$ → Li$_{0.5}$$FeF_3$(t.r.)	Two-phase	[34]
	Li$_{0.5}$$FeF_3$(t.r.) + 0.5Li$^+$ + 0.5e$^-$ → LiF + FeF_2(r.)	Conversion	
LiF + FeF_2 nanocomposite (ball-milled, <5 nm)	(charge) LiF + FeF_2(r.) → FeF_3(r.o.) + Li$^+$ + e$^-$	Reversal conversion	[38]
	(discharge) FeF_3(r.o.) + 0.5Li$^+$ + 0.5e$^-$ → Li$_{0.5}$$FeF_3$(t.r.)	Two-phase	
	Li$_{0.5}$$FeF_3$(t.r.) + xLi$^+$ + xe$^-$ → Li$_{0.5+x}$$FeF_3$(t.r.)	Single-phase ($0 \le x \le 0.5$)	
LiF + FeF_2 nanocomposite (fluorolytic sol-gel, ~10 nm)	(charge) LiF + FeF_2(r.) → FeF_3(r.o.) + Li$^+$ + e$^-$	Reversal conversion	This work
	(discharge) FeF_3(r.o.) + xLi$^+$ + xe$^-$ → Li$_x$$FeF_3$(r.o.)	Single-phase ($0 \le x \le a$)[b]	
	Li$_a$$FeF_3$(r.o.) + $(1-a)$Li$^+$ + $(1-a)$e$^-$ → LiF + FeF_2(r.)	Conversion	

[a]The abbreviations are; r.o.: distorted rhenium trioxide, t.r.: trirutile, and r.: rutile. [b] The upper limit of x, a, is roughly 0.8 according to the GITT measurement.

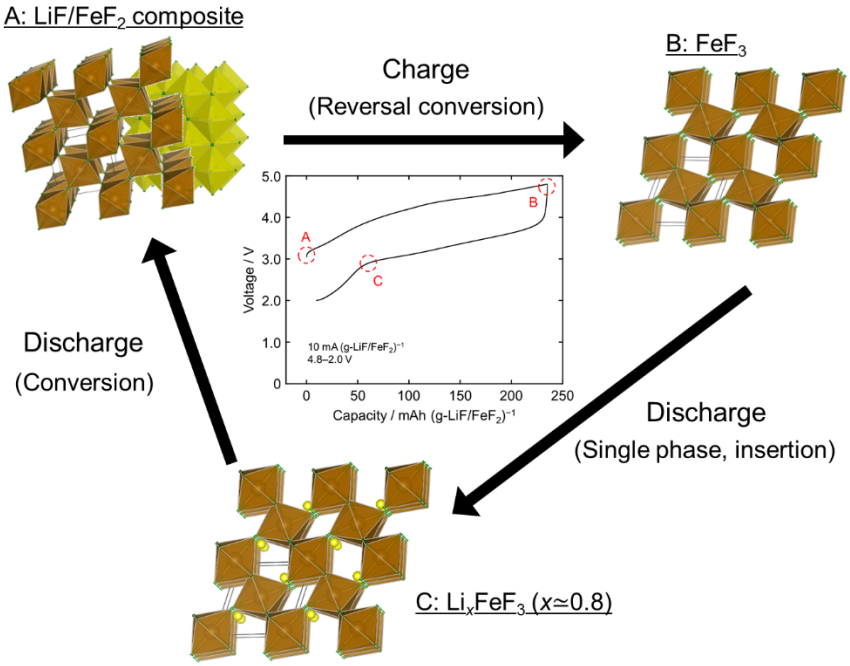

Figure 8 Schematic of the reaction mechanism of the LiF/FeF_2 composite prepared by the fluorolytic sol–gel method (brown octahedron: FeF_6, yellow octahedron: LiF_6, green circle: F, yellow circle: Li).

4. Conclusions

A nanocomposite of LiF and FeF_2 was prepared by a fluorolytic sol–gel method and its charge–discharge behavior as a cathode material for a lithium secondary battery was investigated. The LiF/FeF_2 composite exhibited an initial reversible capacity of 225 mAh $(g\text{-}LiF/FeF_2)^{-1}$ at a current rate of 10 mA $(g\text{-}LiF/FeF_2)^{-1}$, comparable to the theoretical capacity of 227 mAh $(g\text{-}LiF/FeF_2)^{-1}$. Although further improvement of the charge–discharge performance is required, the ease of scaling up the fluorolytic sol–gel preparation method compared with the use of ball-milling makes the composite attractive for mass production. GITT test results revealed a large overpotential during the charging process compared with the discharging process, and the equilibrium potential was approximated by the relaxed potential of the discharging process. The charge–discharge reaction mechanism of the LiF/FeF_2 composite was investigated by XRD, TEM, and XAS. The local structure around the Fe atom was observed to change from that in FeF_2 to that in FeF_3 through the reversal conversion reaction of LiF and FeF_2 during charging, and then back to that in FeF_2 after full discharge. During discharging, Li^+ was first inserted into the rhenium trioxide-type FeF_3 framework to form Li_xFeF_3 ($0 < x < \sim 0.8$), and this was followed by a conversion reaction to reform LiF and FeF_2. The entire reaction

mechanism established from this study provides a new concept of the phase transformation of metal fluoride systems.

Acknowledgements

Two of the authors, S. T. and Y. S., express their gratitude for the financial support of this study by JSPS Research Fellowship for Young Scientists and JSPS KAKENHI (Grant No. 16K05948), respectively.

References

[1] J.B. Goodenough, Y. Kim, Chem. Mater., 22 (2010) 587-603.
[2] V. Etacheri, R. Marom, R. Elazari, G. Salitra, D. Aurbach, Energ. Environ. Sci., 4 (2011) 3243-3262.
[3] J.B. Goodenough, K.-S. Park, J. Am. Chem. Soc., 135 (2013) 1167-1176.
[4] B. Scrosati, J. Hassoun, Y.K. Sun, Energ. Environ. Sci., 4 (2011) 3287-3295.
[5] B. Dunn, H. Kamath, J.M. Tarascon, Science, 334 (2011) 928-935.
[6] Z.G. Yang, J.L. Zhang, M.C.W. Kintner-Meyer, X.C. Lu, D.W. Choi, J.P. Lemmon, J. Liu, Chem. Rev., 111 (2011) 3577-3613.
[7] M.S. Whittingham, Chem. Rev., 104 (2004) 4271-4301.
[8] M.V. Reddy, G.V.S. Rao, B.V.R. Chowdari, Chem. Rev., 113 (2013) 5364-5457.
[9] A.F. Gonzalez, N.H. Yang, R.S. Liu, J. Phys. Chem. C, 121 (2017) 27775-27787.
[10] S.H. Yu, S.H. Lee, D.J. Lee, Y.E. Sung, T. Hyeon, Small, 12 (2016) 2146-2172.
[11] K.F. Chen, D.F. Xue, J. Mater. Chem. A, 4 (2016) 7522-7537.
[12] C. Masquelier, L. Croguennec, Chem. Rev., 113 (2013) 6552-6591.
[13] H. Arai, S. Okada, Y. Sakurai, J. Yamaki, J. Power Sources, 68 (1997) 716-719.
[14] F. Badway, F. Cosandey, N. Pereira, G.G. Amatucci, J. Electrochem. Soc., 150 (2003) A1318-A1327.
[15] H. Li, G. Richter, J. Maier, Adv. Mater., 15 (2003) 736-739.
[16] H. Li, P. Balaya, J. Maier, J. Electrochem. Soc., 151 (2004) A1878-A1885.
[17] I. Plitz, F. Badway, J. Al-Sharab, A. DuPasquier, F. Cosandey, G.G. Amatucci, J. Electrochem. Soc., 152 (2005) A307-A315.
[18] M. Nishijima, I.D. Gocheva, S. Okada, T. Doi, J. Yamaki, T. Nishida, J. Power Sources, 190 (2009) 558-562.
[19] F. Wang, R. Robert, N.A. Chernova, N. Pereira, F. Omenya, F. Badway, X. Hua, M. Ruotolo, R. Zhang, L. Wu, V. Volkov, D. Su, B. Key, M.S. Whittingham, C.P. Grey, G.G. Amatucci, Y. Zhu, J. Graetz, J. Am. Chem. Soc., 133 (2011) 18828-18836.
[20] G.G. Amatucci, N. Pereira, J. Fluorine Chem., 128 (2007) 243-262.
[21] R.E. Doe, K.A. Persson, Y.S. Meng, G. Ceder, Chem. Mater., 20 (2008) 5274-5283.
[22] N. Yamakawa, M. Jiang, B. Key, C.P. Grey, J. Am. Chem. Soc., 131 (2009) 10525-10536.
[23] T. Li, L. Li, Y.L. Cao, X.P. Ai, H.X. Yang, J. Phys. Chem. C, 114 (2010) 3190-3195.
[24] S.-W. Kim, D.-H. Seo, H. Gwon, J. Kim, K. Kang, Adv. Mater., 22 (2010) 5260-5264.
[25] M. Zhou, L. Zhao, T. Doi, S. Okada, J. Yamaki, J. Power Sources, 195 (2010) 4952-4956.

[26] N. Yabuuchi, M. Sugano, Y. Yamakawa, I. Nakai, K. Sakamoto, H. Muramatsu, S. Komaba, J. Mater. Chem., 21 (2011) 10035-10041.
[27] M. Zhou, L. Zhao, A. Kitajou, S. Okada, J. Yamaki, J. Power Sources, 203 (2012) 103-108.
[28] P. Liu, J.J. Vajo, J.S. Wang, W. Li, J. Liu, J. Phys. Chem. C, 116 (2012) 6467-6473.
[29] C. Li, X. Mu, P.A. van Aken, J. Maier, Adv. Energy. Mater., 3 (2013) 113-119.
[30] J. Liu, Y. Wan, W. Liu, Z. Ma, S. Ji, J. Wang, Y. Zhou, P. Hodgson, Y. Li, J. Mater. Chem. A, 1 (2013) 1969-1975.
[31] H.J. Tan, H.L. Smith, L. Kim, T.K. Harding, S.C. Jones, B. Fultz, J. Electrochem. Soc., 161 (2014) A445-A449.
[32] J.K. Ko, K.M. Wiaderek, N. Pereira, T.L. Kinnibrugh, J.R. Kim, P.J. Chupas, K.W. Chapman, G.G. Amatucci, ACS Appl. Mater. Inter., 6 (2014) 10858-10869.
[33] M. Zhou, L. Zhao, S. Okada, J. Yamaki, J. Power Sources, 253 (2014) 74-79.
[34] L. Li, R. Jacobs, P. Gao, L. Gan, F. Wang, D. Morgan, S. Jin, J. Am. Chem. Soc., 138 (2016) 2838-2848.
[35] D. Dambournet, M. Duttine, K.W. Chapman, A. Wattiaux, O. Borkiewicz, P.J. Chupas, A. Demourgues, H. Groult, J. Phys. Chem. C, 118 (2014) 14039-14043.
[36] M. Burbano, M. Duttine, O. Borkiewicz, A. Wattiaux, A. Demourgues, M. Salanne, H. Groult, D. Dambournet, Inorg. Chem., 54 (2015) 9619-9625.
[37] H. Hori, S. Okada, Electrochemistry, 83 (2015) 909-913.
[38] S.-W. Kim, K.-W. Nam, D.-H. Seo, J. Hong, H. Kim, H. Gwon, K. Kang, Nano Today, 7 (2012) 168-173.
[39] K. Erhard, G. Udo, R. Stephan, S.C. Shekar, Angew. Chem. Int. Ed., 42 (2003) 4251-4254.
[40] S. Rüdiger, G. Eltanany, U. Groß, E. Kemnitz, J. Sol-gel Sci. Technol., 41 (2007) 299-311.
[41] J. Kohl, D. Wiedemann, S. Nakhal, P. Bottke, N. Ferro, T. Bredow, E. Kemnitz, M. Wilkening, P. Heitjans, M. Lerch, J. Mater. Chem., 22 (2012) 15819-15827.
[42] S. Tawa, T. Yamamoto, K. Matsumoto, R. Hagiwara, J. Fluorine Chem., 184 (2016) 75-81.
[43] T. Krahl, F. Marroquin Winkelmann, A. Martin, N. Pinna, E. Kemnitz, Chem. Eur. J., 24 (2018) 7177-7187.
[44] A. Martin, M.-L. Doublet, E. Kemnitz, N. Pinna, Adv. Funct. Mater., 28 (2018) 1802057.
[45] S. Brunauer, P.H. Emmett, E. Teller, J. Am. Chem. Soc., 60 (1938) 309-319.
[46] E.P. Barrett, L.G. Joyner, P.P. Halenda, J. Am. Chem. Soc., 73 (1951) 373-380.

[47] T. Taguchi, AIP Conference Proceedings, 882 (2007) 162-164.
[48] J.J. Rehr, R.C. Albers, Rev. Mod. Phys., 72 (2000) 621-654.
[49] A. Tressaud, J. Portier, S. Shearer-Turrell, J.-L. Dupin, P. Hagenmuller, J. Inorg. Nucl. Chem., 32 (1970) 2179-2186.
[50] J. Thewlis, Acta Crystrallogr., 8 (1955) 36-38.
[51] M.J.M. de Almeida, M.M.R. Costa, J.A. Paixao, Acta Crystallogr. B, 45 (1989) 549-555.
[52] P. Scherrer, Nachr. Ges. Wiss. Göttingen, (1918) 98-100.
[53] K.S.W. Sing, D.H. Everett, R.A.W. Haul, L. Moscou, R.A. Pierotti, J. Rouquerol, T. Siemieniewska, Pure. Appl. Chem., 57 (1985) 603-619.
[54] U.C. Srivastava, H.L. Nigam, Coordin. Chem. Rev., 9 (1973) 275-310.
[55] R.D. Shannon, Acta Crystallogr. A, 32 (1976) 751-767.